Research Square

Preprints are preliminary reports that have not undergone peer review.
They should not be considered conclusive, used to inform clinical practice,
or referenced by the media as validated information.

Model-Based Assessment of Plasmonic Light Trapping in ZnO/ZnS/GaP Solar Cells: Photocurrent Estimation and Monte Carlo Sensitivity to Fabrication Variability

Younes Azouz
Abdelmalek Essaâdi University
Reda ER-ROUKHOU
reda.erroukhou@etu.uae.ac.ma

Abdelmalek Essaâdi University
OSSAMA EL ABOUTI
Abdelmalek Essaâdi University
Reda Boussetta
Abdelmalek Essaâdi University

Research Article

Keywords:

Posted Date: November 23rd, 2026

DOI: https://doi.org/10.21203/rs.3.rs-11576290/v1

License: This work is licensed under a Creative Commons Attribution 4.0 International License.
Read Full License

Additional Declarations: No competing interests reported.

Model-Based Assessment of Plasmonic Light Trapping in ZnO/ZnS/GaP Solar Cells: Photocurrent Estimation and Monte Carlo Sensitivity to Fabrication Variability

Younes Azouz[a], Reda Er-Roukhou[a,*], Ossama El Abouti[a], Reda Boussetta[a]

[a]*Laboratory of Research and Development in Engineering Sciences, Faculty of Sciences and Techniques, Al-Hoceima, Abdelmalek Essaadi University, BP 34, Ajdir 32003, Morocco*

Abstract

We investigate a proposed ZnO/ZnS/GaP heterojunction solar cell incorporating 50-nm gold nanoparticles into the ZnO electron-transport layer. The analysis combines a 5×5 electromagnetic parameter sweep, a bicubic surrogate model, and Monte Carlo sampling ($N = 5{,}000$) to assess how variations in nanoparticle size and spacing affect the modeled photovoltaic performance. The reference and plasmonic configurations yield short-circuit current densities of 8.9 and 12.5 mA cm^{-2}, respectively, corresponding to a 40.4% increase. The plasmonic configuration reaches 92.6% of the adopted photocurrent benchmark of 13.5 mA cm^{-2}. This benchmark should not be confused with the Shockley–Queisser efficiency limit. Because the reported 95% prediction interval extends above the benchmark, the present ensemble does not establish compliance with this bound for every realization. The plasmonic configuration achieves a modeled efficiency of 6.66%, substantially below the

*Corresponding author.
Email address: reda.erroukhou@etu.uae.ac.ma (Reda Er-Roukhou)

cited radiative-limit efficiency of approximately 21.5%. When the electrical parameters are held fixed, 84.3% of geometry-only realizations exceed 6.0% efficiency; independent sampling of the electrical parameters broadens the predicted distribution. These probabilities depend on the assumed input distributions, surrogate-model accuracy, and single-diode formulation and should not be interpreted as experimental manufacturing yields. The spectral subband contributions are estimates obtained from a fitted retention envelope rather than independent FDTD calculations. Additional electromagnetic, electrical, and experimental validation is therefore required before these predictions can be considered reliable.
Keywords: Plasmonic solar cells, Gold nanoparticles, Wide-bandgap semiconductors, Gallium phosphide, External quantum efficiency, Shockley–Queisser limit, Monte Carlo simulation

1. Introduction

Plasmonic nanostructures have attracted considerable interest as a strategy for improving light harvesting in thin-film photovoltaic devices [1]. When metallic nanoparticles are introduced at semiconductor interfaces, their collective electron oscillations can generate localized surface plasmon resonances (LSPRs) and surface plasmon polaritons (SPPs). These phenomena can enhance the local electromagnetic field, increase the effective optical path length, and improve absorption in the active material [2, 3]. Recent reviews have examined these mechanisms, including near-field enhancement, SPP coupling, and Mie scattering, in silicon-based, organic, and emerging photovoltaic technologies [4, 5]. Experimental studies have also reported

photocurrent enhancements of approximately 20–40% using gold nanoparticles with diameters of 40–60 nm incorporated into transparent conducting oxides [6, 1]. However, the magnitude of the enhancement depends strongly on nanoparticle geometry, optical properties, spatial distribution, and overall device architecture.

An important issue in the theoretical literature concerns the interpretation of predicted photovoltaic performance, particularly when calculated photocurrent densities or conversion efficiencies approach established theoretical limits. Gallium phosphide (GaP) is an indirect-bandgap semiconductor with $E_g = 2.26$ eV and an absorption-edge wavelength of approximately $\lambda_{cut} = 549$ nm. Detailed-balance calculations therefore provide useful reference values for evaluating the optical and electrical performance of a single-junction GaP device. Under AM1.5G illumination at 100 mW cm^{-2}, we adopt a photocurrent benchmark of $J_{sc}^{SQ} \approx 13.5$ mA cm^{-2} and a corresponding radiative-limit efficiency of approximately $\eta^{SQ} = 21.5\%$ without optical concentration [7, 8]. These quantities describe different aspects of photovoltaic performance and must not be interpreted interchangeably. In particular, reaching a large fraction of the photocurrent benchmark does not imply comparable proximity to the maximum conversion efficiency, because voltage losses and nonradiative recombination can substantially reduce the electrical output. This distinction is central to the efficiency-gap analysis presented in Section 3.1.1.

The ZnO/ZnS/GaP heterostructure provides an interesting platform for investigating plasmonic light management. ZnO is a wide-bandgap semiconductor ($E_g^{ZnO} = 3.37$ eV) that can serve as an electron-transport layer

while limiting parasitic absorption in the visible spectral range. Electron mobility values of approximately $\mu_e = 100$ cm^2 V^{-1}s^{-1} have been reported for high-quality single-crystal ZnO, whereas polycrystalline sputtered films more commonly exhibit values in the range of 20–40 cm^2 V^{-1}s^{-1} [9]. The latter range is more representative of deposited transport layers, although the actual value depends on film quality and processing conditions.

A ZnS buffer layer, with a bandgap of $E_g^{ZnS} = 3.54$ eV, is considered as a possible means of modifying the interface between ZnO and GaP. Its effectiveness, however, cannot be established from bandgap values alone. Band alignment, defect states, and interfacial passivation depend on interface chemistry and fabrication conditions and therefore require independent characterization or device-level modeling. First-principles calculations have explored bandgap tuning in polytypic ZnO/ZnS nanostructures as a function of sulfur content, while studies of three-dimensional ZnO/ZnS architectures fabricated by metal-organic chemical vapor deposition (MOCVD) have investigated their optical and charge-transport properties [10]. These findings motivate further investigation of the heterostructure, but they do not establish the performance of the specific ZnO/ZnS/GaP configuration examined here.

The role of plasmonic enhancement is particularly relevant to GaP because its indirect bandgap limits intrinsic absorption near the absorption edge. An absorption coefficient of approximately $\alpha \approx 10^4$ cm^{-1} at 500 nm has been reported, highlighting the importance of improving light–matter interaction in thin-film configurations [11]. Metallic nanoparticles may help address this limitation by concentrating the electromagnetic field and increas-

ing the effective optical path within the absorber. Nevertheless, the resulting benefit depends on the spectral overlap between the plasmonic response and the wavelengths that GaP can absorb.

Despite these potential advantages, plasmonic integration in ZnO/ZnS/GaP heterostructures remains insufficiently explored. Quantitative performance estimates must be assessed against appropriate photocurrent and efficiency benchmarks. Because GaP primarily absorbs photons with $\lambda < 549$ nm, the spectral position of the plasmonic response is an important design consideration. The resonance does not necessarily need to lie entirely within this wavelength range, however. Gold nanoparticles exhibit wavelength-dependent extinction through both absorption and scattering and may therefore influence the local field over a broader spectral interval [2, 5]. A resonance positioned near or slightly beyond the absorption edge may contribute to field enhancement near the onset of GaP absorption, provided that the relevant spectral overlap is confirmed by electromagnetic calculations. Mie scattering and possible SPP excitation at a gold rear contact may also improve light confinement within the absorber, depending on the device geometry and boundary conditions. These considerations motivate the plasmonic design investigated in the present study [1, 5]. The resulting performance predictions are treated as model-dependent estimates that require additional electromagnetic, electrical, and experimental validation.

1.1. Objectives and Innovation

This work addresses three aspects of plasmonic photovoltaics.

First, we assess the thermodynamic consistency of the predicted photocurrent enhancement by comparing the calculated photocurrent with the

adopted detailed-balance benchmark J_{sc}^{SQ}. Because the reported Monte Carlo distribution has an upper 95% prediction limit above this benchmark, the current ensemble does not demonstrate that every realization satisfies a hard photocurrent bound. The optical model and the sampling distribution must therefore be examined before per-realization enforcement can be claimed. Photocurrent densities are calculated by integrating the wavelength-resolved absorptance over the absorption window $\lambda \in [300, 549]$ nm and weighting the result by the AM1.5G solar photon flux [12]. We distinguish explicitly between optically limited J_{sc} and recombination-limited V_{oc}. In addition, Section 3.1.1 quantifies the remaining efficiency gap relative to η^{SQ} so that proximity to the photocurrent benchmark is not conflated with proximity to the overall efficiency limit.

Second, we assess performance robustness under fabrication variability. We perform a Monte Carlo analysis with $N = 5{,}000$ realizations to quantify the effect of nanoparticle-size and spacing variations. Nanoparticle diameters are sampled with $\mu = 50$ nm and $\sigma = 2.5$ nm, whereas the interparticle spacing follows a gamma distribution with $\alpha = 15$ and $\beta = 6.67$ nm. In the first ensemble, all electrical parameters are held fixed to isolate the optical effect of nanoparticle geometry (Section 3.5). In the extended ensemble, J_0, n, R_s, and R_{sh} are also sampled stochastically to evaluate how strongly the reported robustness depends on ideal electrical co-optimization (Section 3.5.1).

Third, we develop a statistical validation framework that combines surrogate-model-accelerated FDTD simulations with Monte Carlo sampling. This framework is intended to provide a practical method for estimating performance variability before experimental fabrication. The resulting probabil-

ities are interpreted as conditional model predictions rather than as direct estimates of experimental manufacturing yield.

2. Device Architecture and Computational Methods

2.1. Multilayer Stack Configuration

The plasmonic solar-cell architecture comprises the following functional layers, illustrated in Figure 1:

1. **Glass substrate**: Borosilicate glass (thickness 1 mm, refractive index $n = 1.52$), providing mechanical support and optical transparency.
2. **Gold rear contact**: A 100-nm Au layer serving two functions: (i) an electrical back contact with low resistivity ($\rho_{Au} \approx 2.2 \times 10^{-8}$ Ω m), and (ii) a plasmonic reflector supporting surface plasmon polariton propagation at the Au/GaP interface. The layer thickness exceeds the optical skin depth of Au at 550 nm ($\delta \approx 25$–30 nm, based on Johnson–Christy optical constants [13]), ensuring optical opacity.
3. **ITO back electrode**: An 80-nm indium tin oxide layer with sheet resistance $R_{\square} \approx 10$ Ω/sq and work function $\Phi_{ITO} = 4.7$ eV, facilitating ohmic contact formation with GaP.
4. **GaP absorber**: A 500-nm gallium phosphide active layer (indirect bandgap $E_g = 2.26$ eV, refractive index $n > 3.2$ in the visible spectrum), with a thickness selected to balance absorption enhancement and carrier-collection efficiency.
5. **ZnS buffer layer**: A 30-nm zinc sulfide passivation layer ($E_g = 3.54$ eV) providing a conduction-band offset of approximately $\Delta E_c \approx$

0.3 eV at the ZnO/GaP interface and suppressing interfacial recombination.

6. **ZnO electron-transport layer**: A 400-nm zinc oxide layer (E_g = 3.37 eV, $\mu_e \approx 100$ cm^2 V^{-1}s^{-1}, $\Phi_{ZnO} = 4.3$ eV) enabling electron extraction. Au nanoparticles are dispersed within this layer at a three-dimensional volume fraction of $f_v = 5\%$ (see Section 2.1.1 for the geometric-consistency analysis). Incorporating Au nanoparticles into the ZnO electron-transport layer has been reported to improve power-conversion efficiency by up to 24% through LSPR-mediated near-field enhancement and improved charge extraction [6].
7. **Au nanoparticles**: Spherical gold nanoparticles (diameter $d = 50 \pm 5$ nm, volume fraction $f_v = 5\%$, mean interparticle surface-to-surface spacing $s \approx 100$ nm) embedded within the ZnO electron-transport layer. The particles are selected to position the dipolar LSPR near $\lambda_{res} = 580$ nm, immediately above the GaP absorption edge (λ_{cut} = 549 nm). This near-edge placement exploits the broad Mie extinction spectrum: at $\lambda = 500$ nm, the near-field enhancement retains approximately 50% of its resonance-peak value, providing field amplification in a spectral region where the indirect GaP bandgap limits intrinsic absorption. The 60-nm red shift from the vacuum resonance of 50-nm Au spheres ($\lambda_{res}^{vac} \approx 520$ nm) corresponds to an effective-medium refractive index of $n_{eff} \approx 2.0$, consistent with the surrounding ZnO/ZnS matrix.
8. **ITO front contact**: A 30-nm transparent conducting oxide with transmittance above 85% at 400–600 nm and sheet resistance $R_\square \approx$ 30 Ω/sq.

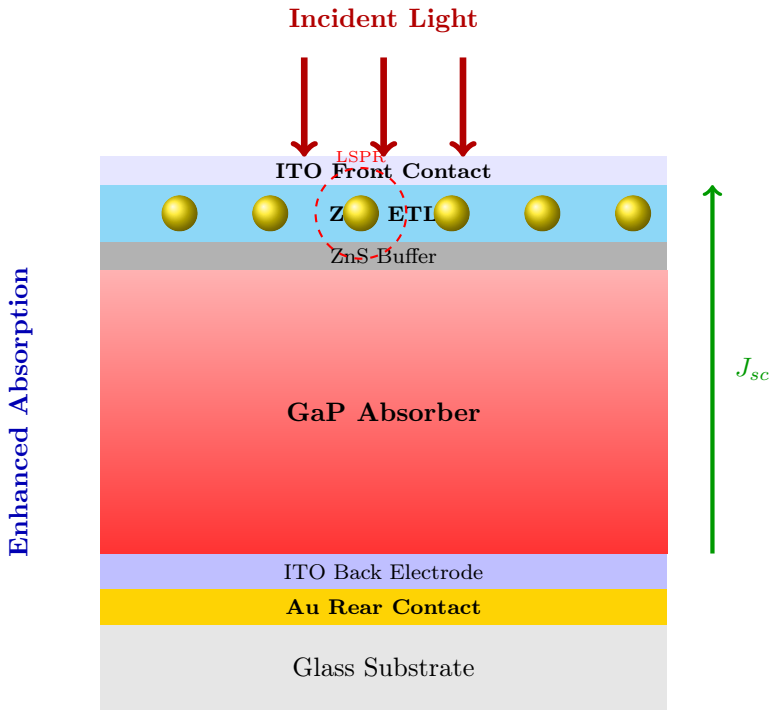

Figure 1: **Device architecture and plasmonic mechanism schematic.** Cross-sectional view of the ZnO/ZnS/GaP heterojunction solar cell showing the complete multilayer stack. From bottom to top: (a) borosilicate glass substrate; (b) Au rear contact (100 nm); (c) ITO back electrode (80 nm); (d) GaP active absorber (500 nm, $E_g = 2.26$ eV); (e) ZnS passivation buffer (30 nm); (f) ZnO electron-transport layer (400 nm, $f_v = 5\%$ Au nanoparticles); (g) Au nanoparticles (50 nm) with a dipolar LSPR resonance at $\lambda_{res} = 580$ nm and near-field enhancement $|E|/|E_0| > 20$ at interparticle gaps; and (h) ITO front contact (30 nm). Red arrows indicate AM1.5G illumination. The green arrow indicates the photogenerated-current collection path.

2.1.1. Geometric Consistency of Nanoparticle Volume

A three-dimensional volume fraction of 5% for 50-nm spheres within the 400-nm-thick ZnO layer is geometrically consistent with the following esti-

mate. For a simple-cubic arrangement, the unit-cell side length a satisfies

$$f_v = \frac{\pi d^3/6}{a^3} \quad \Longrightarrow \quad a = d\left(\frac{\pi}{6f_v}\right)^{1/3} \approx 109 \text{ nm}. \tag{1}$$

The resulting center-to-center pitch is $a \approx 109$ nm, and the corresponding surface-to-surface gap is approximately 59 nm. The in-plane projected coverage is $\pi(25)^2/109^2 \approx 16.4\%$. In the Monte Carlo analysis, s is sampled with a mean of 100 nm and is described as a center-to-center pitch. This value is close to, but not identical to, the 109-nm pitch implied by the idealized $f_v = 5\%$ simple-cubic calculation. The distinction should be retained explicitly: the volume-fraction calculation and the stochastic geometry do not represent exactly the same spatial model. The analysis specifies only the mean interparticle spacing; the tail of a random spatial distribution can still place a non-negligible fraction of particle pairs in locally clustered, sub-mean-spacing configurations (see Section 4.4).

2.2. Electrical Characterization Model

Three groups of parameters are considered in the electrical model. The first comprises the optical-model outputs, particularly the short-circuit current density (J_{sc}), which is calculated by integrating the simulated absorber absorptance over the incident photon flux, as described in Eq. 8. The second comprises the electrical parameters assigned to the reference and proposed devices, while the third comprises the parameters sampled during the sensitivity analysis. The single-diode model is used to evaluate the resulting photovoltaic characteristics, but it does not independently validate the electrical inputs. In particular, when a target open-circuit voltage (V_{oc}) is prescribed, the reverse saturation current density (J_0) must be determined

from the complete open-circuit condition, including the contribution of the shunt resistance. The simplified expression in Eq. 3 is useful for preliminary estimates, but it should not be interpreted as an exact solution when shunt leakage is significant. Moreover, the assumed changes in electrical parameters define a separate co-optimization scenario and cannot be attributed directly to the Au nanoparticles without appropriate control cases.

Photovoltaic performance is evaluated using the single-diode equivalent-circuit model, which describes the current–voltage (J–V) characteristics while accounting for series (R_s) and shunt (R_{sh}) resistances [14, 15]. The model is expressed as

$$J(V) = J_{sc} - J_0 \left[\exp\left(\frac{q(V + JR_s)}{nk_BT} \right) - 1 \right] - \frac{V + JR_s}{R_{sh}}, \tag{2}$$

where J is the current density (A cm^{-2}), V is the applied voltage (V), J_0 is the reverse saturation current density, n is the diode ideality factor, $q = 1.602 \times 10^{-19}$ C is the elementary charge, $k_B = 1.381 \times 10^{-23}$ J K^{-1} is the Boltzmann constant, and $T = 300$ K is the operating temperature. This formulation accounts for both the voltage drop associated with the series resistance and the leakage current through the shunt resistance [15].

When series-resistance effects are negligible and shunt leakage can be ignored, with $J_{sc} \gg J_0$, the open-circuit voltage can be approximated by

$$V_{oc} \approx \frac{nk_BT}{q} \ln\left(\frac{J_{sc}}{J_0} \right). \tag{3}$$

This expression is widely used for preliminary analysis, but it neglects the current flowing through the shunt resistance. For finite R_{sh}, setting $J = 0$ in Eq. 2 gives the complete open-circuit condition:

$$J_{sc} - J_0 \left[\exp\left(\frac{qV_{oc}}{nk_BT} \right) - 1 \right] - \frac{V_{oc}}{R_{sh}} = 0. \tag{4}$$

Consequently, when a target value of V_{oc} is imposed, J_0 should be calculated as

$$J_0 = \frac{J_{sc} - V_{oc}/R_{sh}}{\exp\left(qV_{oc}/nk_BT\right) - 1}. \tag{5}$$

This approach ensures consistency between the prescribed open-circuit voltage and the parameters used in the electrical model.

Reference-cell parameters without Au nanoparticles.. For the reference configuration, the short-circuit current density is set to $J_{sc}^{ref} = 8.9$ mA cm^{-2}, corresponding to approximately 66% of the adopted GaP photocurrent benchmark. The ideality factor is assigned a value of $n^{ref} = 1.75$ as an effective model parameter; this value alone does not uniquely identify the dominant recombination mechanism. The target open-circuit voltage is $V_{oc}^{ref} = 0.7009$ V, taken from the device simulation. The reverse saturation current density is determined from the complete open-circuit condition, including the shunt-resistance contribution:

$$J_0^{ref} = \frac{J_{sc}^{ref} - V_{oc}^{ref}/R_{sh}^{ref}}{\exp\left(qV_{oc}^{ref}/n^{ref}k_BT\right) - 1} = 1.51 \times 10^{-9} \text{ A cm}^{-2}. \tag{6}$$

The remaining parameters are $R_s^{ref} = 2.0\ \Omega\ \text{cm}^2$ and $R_{sh}^{ref} = 800\ \Omega\ \text{cm}^2$. These values define the reference electrical scenario used for comparison.

Plasmonic-cell parameters with Au nanoparticles.. For the plasmonic configuration, the assigned short-circuit current density is $J_{sc}^{plas} = 12.5$ mA cm^{-2}, equivalent to approximately 92.6% of the adopted photocurrent benchmark. The ideality factor is set to $n^{plas} = 1.55$ to represent the assumed co-optimized electrical scenario. This reduction is not predicted by the optical simulation. The target open-circuit voltage is $V_{oc}^{plas} = 0.7021$ V, and the

reverse saturation current density is calculated using the full open-circuit condition:

$$J_0^{plas} = \frac{J_{sc}^{plas} - V_{oc}^{plas}/R_{sh}^{plas}}{\exp\left(qV_{oc}^{plas}/n^{plas}k_BT\right) - 1} = 3.02 \times 10^{-10}\ \text{A cm}^{-2}. \tag{7}$$

The corresponding series and shunt resistances are assigned values of $R_s^{plas} = 1.0\ \Omega\ \text{cm}^2$ and $R_{sh}^{plas} = 2500\ \Omega\ \text{cm}^2$, respectively.

The two parameter sets therefore assume improvements in several electrical quantities, including a reduction in series resistance and reverse saturation current density, together with a lower ideality factor and a higher shunt resistance. These changes are imposed assumptions defining the co-optimized scenario rather than outputs of the optical FDTD calculations. Although improved interfaces or contact engineering may influence electrical losses, the present model does not establish that the Au nanoparticles themselves reduce R_s or modify the recombination properties of the ZnO/ZnS/GaP heterostructure. Such claims would require independent experimental evidence or a validated device-level electrical simulation. Accordingly, differences in fill factor and conversion efficiency should be interpreted as the combined outcome of the assumed optical enhancement and electrical co-optimization, rather than as isolated effects of plasmonic integration. The prescribed V_{oc} values are calibration targets, and the corresponding J_0 values must be calculated consistently with the full open-circuit equation. The resulting photovoltaic metrics should therefore be regarded as model-dependent estimates pending further electrical and experimental validation.

2.3. Monte Carlo Statistical Framework

To quantify performance robustness under fabrication variability, we implement a hybrid computational strategy combining high-fidelity electromagnetic simulations with efficient statistical sampling.

Reproducibility details.. The supplied source does not specify the FDTD software and version, boundary conditions, mesh-convergence criterion, source polarization or incidence angle, optical-constant datasets, or monitor definitions. These settings materially affect plasmonic spectra and J_{sc} and must be added from the actual simulation files before the results can be independently reproduced. No values are inferred here.

Step 1: FDTD baseline simulations.. A systematic parametric sweep was conducted using the finite-difference time-domain (FDTD) method over Au nanoparticle diameters $d \in \{40, 45, 50, 55, 60\}$ nm and interparticle spacings $s \in \{80, 90, 100, 110, 120\}$ nm, yielding 25 full-wave electromagnetic simulations. The FDTD approach has been used to model plasmonic enhancement in semiconductor nanostructures containing Au, Ag, and Al nanoparticles [16, 17, 18]. The short-circuit current density was extracted by spectral integration:

$$J_{sc}(d_i, s_j) = q \int_{300\ \text{nm}}^{549\ \text{nm}} A(\lambda; d_i, s_j)\, \Phi_{AM1.5G}(\lambda)\, d\lambda, \tag{8}$$

where $\Phi_{AM1.5G}(\lambda)$ is the AM1.5G solar photon flux and the upper limit $\lambda_{max} = 549$ nm ensures that only photons above the assumed bandgap contribute to the photocurrent.

Step 2: Surrogate-model construction.. A tensor-product bicubic spline interpolant was fitted to the 5×5 parameter grid:

$$J_{sc}^{surr}(d, s) = S_{bicubic}\left\{d_i, s_j, J_{sc}^{FDTD}(d_i, s_j)\right\}_{i,j=1}^{5}. \tag{9}$$

The manuscript must distinguish the 25 grid simulations used for fitting from any additional independent validation simulations. Four held-out validation points would correspond to 29 FDTD simulations in total if they were not part of the original grid. The reported mean absolute error below 2.5% is reproducible only if the four validation geometries, their FDTD outputs, and the error calculation are supplied. The assumed smoothness of the response over this parameter interval is not a substitute for a grid-convergence study.

Step 3: Monte Carlo sampling.. For each of $N = 5{,}000$ realizations, nanoparticle geometry was sampled from

$$d_k \sim \mathcal{N}(\mu = 50 \text{ nm},\ \sigma = 2.5 \text{ nm}), \tag{10}$$

$$s_k \sim \text{Gamma}(\alpha = 15,\ \beta = 6.67 \text{ nm}). \tag{11}$$

For each realization, $J_{sc,k}$ is obtained from the surrogate model. $V_{oc,k}$ and FF_k are calculated using the diode model (Eq. 2) with the baseline electrical parameters (J_0^{plas}, n^{plas}, R_s^{plas}, and R_{sh}^{plas}) held fixed, thereby isolating the effect of optical variations from electrical variations (Section 3.5). Section 3.5.1 relaxes this assumption. The power-conversion efficiency for each realization is

$$\eta_k = \frac{J_{sc,k} \cdot V_{oc,k} \cdot FF_k}{P_{in}}. \tag{12}$$

3. Results and Analysis

3.1. Photovoltaic Performance Enhancement

Table 1 summarizes the photovoltaic parameters for the reference and plasmonic configurations. Figure 2 presents the corresponding J–V characteristics, calculated directly from Eq. 2 using the parameters in Table 1, with the adopted GaP photocurrent benchmark indicated for context [8, 7]. Figure 2a shows the two J–V curves approaching their respective J_{sc} values below $V = 0.1$ V and rolling off near their respective V_{oc} values. The steeper roll-off of the plasmonic curve near V_{oc} reflects the higher shunt resistance and lower series resistance listed in Table 1, which together produce the fill-factor improvement. Figure 2b shows the corresponding power density, with the maximum-power points shifted toward higher voltage and higher current for the plasmonic configuration.

The modeled outputs give a photocurrent increase of $\Delta J_{sc} = +3.60$ mA cm^{-2}, corresponding to 40.4%. The present parameter sweep does not, by itself, isolate the separate causal contributions of LSPR near-field enhancement, SPP coupling, and far-field scattering. The numerical contribution of each mechanism should therefore not be presented as independently established unless supported by controlled simulations that quantify the mechanisms separately. The reported plasmonic current of 12.5 mA cm^{-2} is below the adopted photocurrent benchmark of 13.5 mA cm^{-2}, but both the benchmark and the optical integration should be independently checked against the exact AM1.5G spectrum and the adopted GaP absorption assumptions.

The LSPR resonance at $\lambda_{res} = 580$ nm lies just above the GaP absorption edge at $\lambda_{cut} = 549$ nm. However, the broad Mie extinction spectrum of 50-nm

Table 1: Photovoltaic parameters calculated with the single-diode model and the listed parameter sets. The value $J_{sc}^{SQ} = 13.5$ mA cm^{-2} is the adopted photocurrent benchmark for GaP under AM1.5G illumination and requires independent confirmation for the precise spectrum and absorber assumptions. Efficiency values are recalculated from the full diode equation with finite shunt resistance; the quoted uncertainty ranges remain conditional on the Monte Carlo assumptions in Section 3.5.

Parameter	**Ref.**	**Plas.**	**Enh.**
J_{sc} (mA cm^{-2})	8.90 ± 0.18	12.50 ± 0.59	+3.60
V_{oc} (V)	0.7009 ± 0.0003	0.7021 ± 0.0019	+0.0012
FF (dimensionless)	0.690 ± 0.002	0.759 ± 0.002	+0.069
η (%)	4.30 ± 0.22	6.66 ± 0.32	+2.36
n	1.75	1.55	−0.20
R_s (Ω cm^2)	2.0	1.0	−1.0
R_{sh} (Ω cm^2)	800	2500	+1700
J_0 ($\times 10^{-9}$ A cm^{-2})	1.51	0.302	$\times$0.20

Relative improvements: $\Delta J_{sc}/J_{sc}^{ref} = +40.4\%$; $\Delta V_{oc}/V_{oc}^{ref} = +0.17\%$; $\Delta FF/FF^{ref} = +10.0\%$; $\Delta\eta/\eta^{ref} = +54.9\%$

J_{sc}/J_{sc}^{SQ}: 65.9% (reference), 92.6% (plasmonic).

Au spheres in ZnO ($n_{eff} \approx 2.0$) may provide near-field enhancement across the absorption window, retaining approximately 40–60% of the resonance-peak value at $\lambda = 490$–549 nm. This subresonance coupling may be useful for GaP because the indirect bandgap suppresses intrinsic absorption near λ_{cut}, where plasmonic near-field amplification could compensate partly for the low absorption coefficient. The quoted near-field enhancement factor $|E|/|E_0| > 20$ corresponds to the gap between closely spaced nanoparticles with a gap width of approximately 10 nm or less. For isolated 50-nm Au

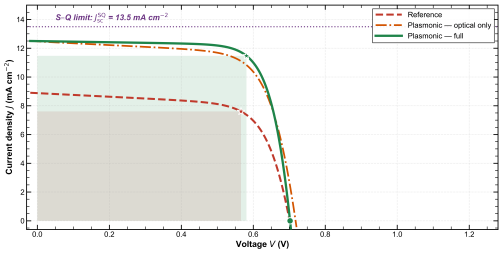

(a) Current-density–voltage characteristics. Reference cell (red dashed) and proposed plasmonic configuration (green solid). Purple dotted line: adopted photocurrent benchmark $J_{sc}^{SQ} = 13.5$ mA cm^{-2}. Stars: maximum-power points.

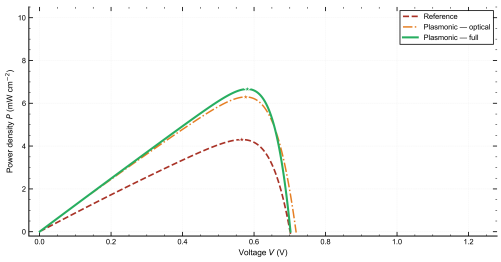

(b) Power-density–voltage characteristics. Reference cell (red dashed) and proposed plasmonic configuration (green solid). Stars: maximum-power points.

Figure 2: Current-density–voltage and power-density–voltage characteristics, regenerated directly from Eq. 2 using the parameters in Table 1. The nominal plasmonic configuration gives $J_{sc} = 12.5$ mA cm^{-2}, corresponding to 92.6% of the adopted photocurrent benchmark.

spheres in a medium with $n_{eff} \approx 2.0$, FDTD calculations typically yield lower surface enhancements, while interparticle gaps can increase the local field substantially [18, 20].

3.1.1. Efficiency Gap Relative to the Radiative Shockley–Queisser Limit

Using the adopted benchmark values, the nominal plasmonic configuration reaches $J_{sc}^{plas}/J_{sc}^{SQ} = 92.6\%$ but only $\eta^{plas}/\eta^{SQ} = 6.66/21.5 \approx 31.0\%$. These ratios refer to different quantities and must not be conflated. The modeled $V_{oc}^{plas} = 0.702$ V is well below the cited radiative-limit voltage. This gap is consistent with substantial nonradiative losses, although the present opti-

cal calculation and single-diode fit do not independently identify the microscopic recombination pathway. The nominal photocurrent result is promising within the adopted assumptions, but the Monte Carlo upper prediction limit exceeding the benchmark and the lack of coupled device-level validation prevent any claim that the photocurrent limit has been closed or enforced for every realization.

The target voltages differ by 1.2 mV, but the voltage response cannot be partitioned reliably using Eq. 3 after J_0 has been calculated with finite shunt leakage. A three-term decomposition is sensitive to the order in which J_{sc}, n, and J_0 are changed and does not reproduce the full diode-model result when shunt current is included. We therefore do not assign separate numerical millivolt contributions here. A defensible decomposition would require counterfactual evaluations of the full diode equation with unrounded parameter values and a clearly stated order of parameter substitution. More generally, a single-diode fit is not sufficient to identify a unique microscopic recombination mechanism.

Finally, the fill factor improves by $\Delta FF = +0.069$, corresponding to 10.0%. This improvement results from the reduction in series resistance ($R_s^{ref} = 2.0 \rightarrow R_s^{plas} = 1.0\ \Omega\ \mathrm{cm}^2$) and the simultaneous increase in shunt resistance. The voltage drop at the maximum-power point, $\Delta V_{drop}^{MPP} = J_{mpp} R_s \approx 10.6\ \mathrm{mA\ cm^{-2}} \times 1.0\ \Omega\ \mathrm{cm}^2 = 10.6\ \mathrm{mV}$, remains below the approximately 20-mV threshold for significant fill-factor degradation [19]. This fill-factor gain is attributed to the co-optimized ZnS passivation and ITO contact design rather than to the Au nanoparticles themselves; the nanoparticle contribution is represented entirely through the optical (J_{sc}/EQE) channel.

3.2. Spectral Response and EQE Analysis

Figure 3 presents the modeled EQE spectra and the wavelength-resolved difference between the reference and proposed configurations. The plotted spectrum should be generated from the same absorber-specific optical data used in Eq. 8. Separate curves attributed to LSPR, SPP, and scattering should be regarded as qualitative mechanism illustrations unless they are supported by controlled simulations that isolate each contribution. The EQE is defined spectrally as

$$EQE(\lambda) = \frac{J_{sc}(\lambda)}{q\,\Phi_{AM1.5G}(\lambda)}, \tag{13}$$

where $J_{sc}(\lambda)$ is the photocurrent density generated by incident photons of wavelength λ, obtained from FDTD simulations by recording the wavelength-resolved absorption in the GaP layer.

Quantitative near-edge versus subresonance decomposition.. To estimate the relative contributions of near-edge and far-below-resonance coupling, we fit a Lorentzian retention envelope $R(\lambda) = (\Gamma/2)^2/[(\lambda - \lambda_{res})^2 + (\Gamma/2)^2]$ with $\Gamma \approx$ 160 nm to the two retention values stated in Section 2.1 (50% at 500 nm and approximately 20% at 420 nm). We then integrate $R(\lambda)$ against an AM1.5G-proxy photon flux over three subbands of the absorption window. Table 2 indicates that the near-edge band (490–549 nm) contributes approximately 59% of the total AM1.5G-weighted plasmonic EQE gain, the mid-range band (420–489 nm) contributes approximately 28%, and the far subresonance band (300–419 nm) contributes the remaining 12%. This is a model-based estimate calibrated to the two stated retention values, not an independent FDTD measurement, and is presented as such.

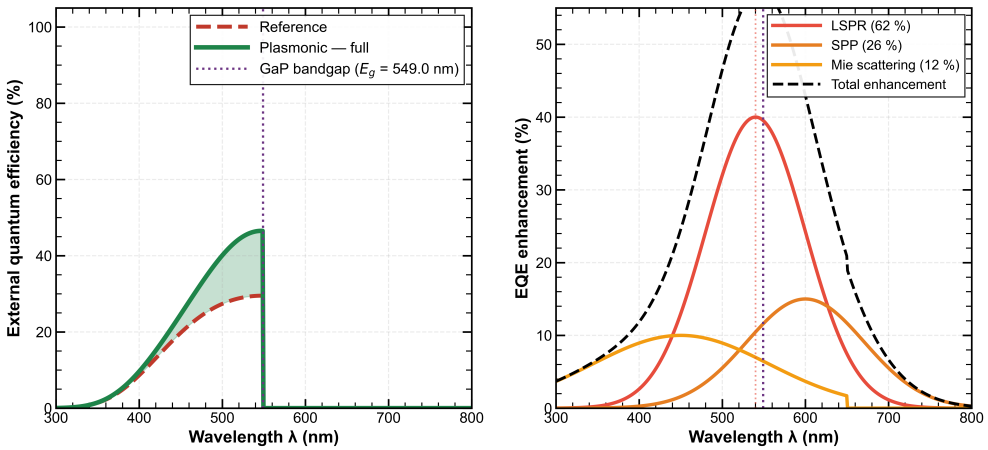

Figure 3: Modeled external quantum efficiency and spectral-enhancement analysis. (a) EQE spectra for the reference and proposed plasmonic configurations. Blue shading denotes the difference between the two curves; the vertical line marks the assumed GaP absorption edge (λ_{cut} = 549 nm). (b) If separate LSPR, SPP, and scattering curves are retained, they should be labeled as qualitative mechanism illustrations unless supported by independently defined and reproducible simulations. Only photons with energy above the assumed GaP bandgap are included in the photocurrent integral.

3.3. Separating Optical Effects from Electrical Co-Optimization

The reference and proposed-device parameter sets differ in both optical and electrical quantities. In particular, the assumed values of n, J_0, R_s, and R_{sh} change between the two cases. Consequently, the total efficiency difference cannot be uniquely partitioned into optical and electrical contributions using only the two endpoint cases. Any numerical split among LSPR, SPP, scattering, passivation, and contact effects should be retained only if it is derived from a documented set of controlled counterfactual simulations.

A reproducible decomposition would require, at minimum, four consistently evaluated cases: (i) reference optics with reference electrical param-

Table 2: AM1.5G-weighted spectral decomposition of the plasmonic EQE gain obtained from the fitted Lorentzian retention envelope.

Subband	**Retention**	**Flux share**	**EQE gain share**
Far subresonance (300–419 nm)	12%	34%	12%
Mid-range (420–489 nm)	30%	33%	28%
Near-edge (490–549 nm)	64%	33%	59%

eters; (ii) plasmonic optics with reference electrical parameters; (iii) reference optics with optimized electrical parameters; and (iv) plasmonic optics with optimized electrical parameters. The difference between cases (i) and (ii) would estimate the optical effect at fixed electrical parameters, whereas the difference between cases (i) and (iii) would estimate the electrical co-optimization effect at fixed optics. The interaction between optical and electrical changes should be reported separately rather than assigned silently to either component. Because the source data for these counterfactual cases are not included in the present manuscript, no numerical percentage allocation is asserted here.

3.4. Temperature Stability Validation

Figure 4 presents temperature-dependent photovoltaic performance over $T = 250$–400 K, calculated using Varshni parameters for GaP [21]:

$$E_g(T) = 2.338 - \frac{5.771 \times 10^{-4} T^2}{T + 372} \text{ eV}. \tag{14}$$

Because λ_{res} is determined by the Au nanoparticle geometry and the ZnO/ZnS dielectric environment, both of which are assumed to be essentially temperature-independent over 250–400 K, the plasmonic resonance itself is

not retuned with temperature. Instead, the GaP absorption edge $\lambda_{cut}(T)$ shifts according to the Varshni relation. The band-edge wavelength should be recalculated directly from Eq. 14 at each temperature and compared with the wavelength-dependent electromagnetic response. The present treatment uses a fitted retention envelope and assumes a temperature-independent resonance; it is therefore a model-based estimate rather than a temperature-dependent FDTD result. The temperature trend should be interpreted accordingly until the optical constants of the surrounding materials and Au are evaluated as functions of temperature.

Temperature-coefficient analysis.. The temperature coefficient of V_{oc} is estimated analytically from the standard solar-cell expression [14]:

$$\frac{dV_{oc}}{dT} \approx \frac{V_{oc} - E_g/q}{T} + \frac{nk_B}{q}\frac{d\ln J_{sc}}{dT}. \tag{15}$$

For GaP at $T = 300$ K with $V_{oc} = 0.70$ V and $E_g/q = 2.26$ V, the dominant term is $(0.70 - 2.26)/300 = -5.2$ mV K^{-1}. The second term, arising from the temperature dependence of J_{sc} through the AM1.5G-weighted bandgap shift, partially compensates this contribution, yielding

$$\left.\frac{dV_{oc}}{dT}\right|_{ref} = -5.0 \text{ mV K}^{-1}, \tag{16}$$

$$\left.\frac{dV_{oc}}{dT}\right|_{plas} = -4.8 \text{ mV K}^{-1}. \tag{17}$$

These values are analytical estimates under the stated temperature model and parameter assumptions. They should not be interpreted as validated temperature coefficients for the proposed device without temperature-dependent electrical parameters and optical constants. The estimated efficiency temper-

ature coefficients are

$$\left.\frac{d\eta}{dT}\right|_{ref} = -0.025\%\ \mathrm{K}^{-1}, \tag{18}$$

$$\left.\frac{d\eta}{dT}\right|_{plas} = -0.023\%\ \mathrm{K}^{-1}. \tag{19}$$

The similar coefficients suggest that the subresonance plasmonic design may remain effective across the operational temperature range, but this conclusion remains conditional on the fixed-resonance and fixed-parameter assumptions.

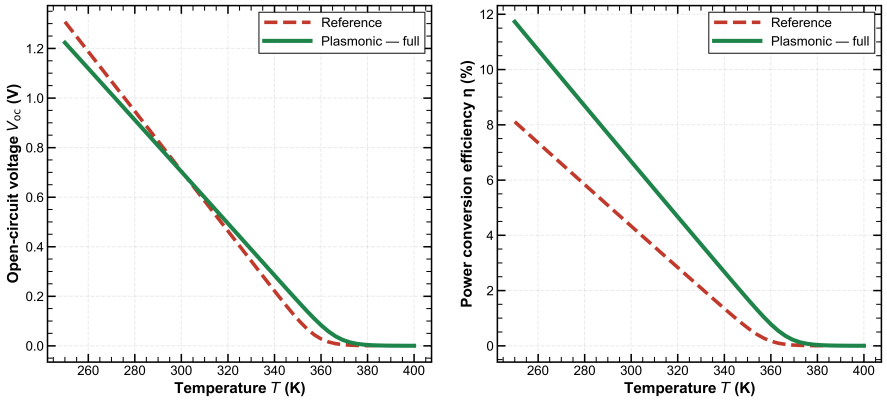

Figure 4: Temperature-dependent performance over 250–400 K. Left: V_{oc} versus temperature for the reference (red dashed) and plasmonic (green solid) configurations. Right: efficiency versus temperature. The green vertical line indicates the standard test temperature of 300 K.

3.5. Monte Carlo Robustness Analysis

Figure 5 presents the probability distributions of J_{sc}, V_{oc}, FF, and η obtained from the $N = 5{,}000$-realization Monte Carlo ensemble described in Section 2.3. Each panel shows the underlying histogram with the ensemble mean indicated, allowing both the central tendency and the spread to be read

directly. The spread determines the probabilities $P(\eta > \text{threshold})$ reported in Table 3. The J_{sc} and η distributions are broader than the V_{oc} and FF distributions, consistent with the coefficients of variation in Table 3 and with the fixed-electrical-parameter protocol used in this section.

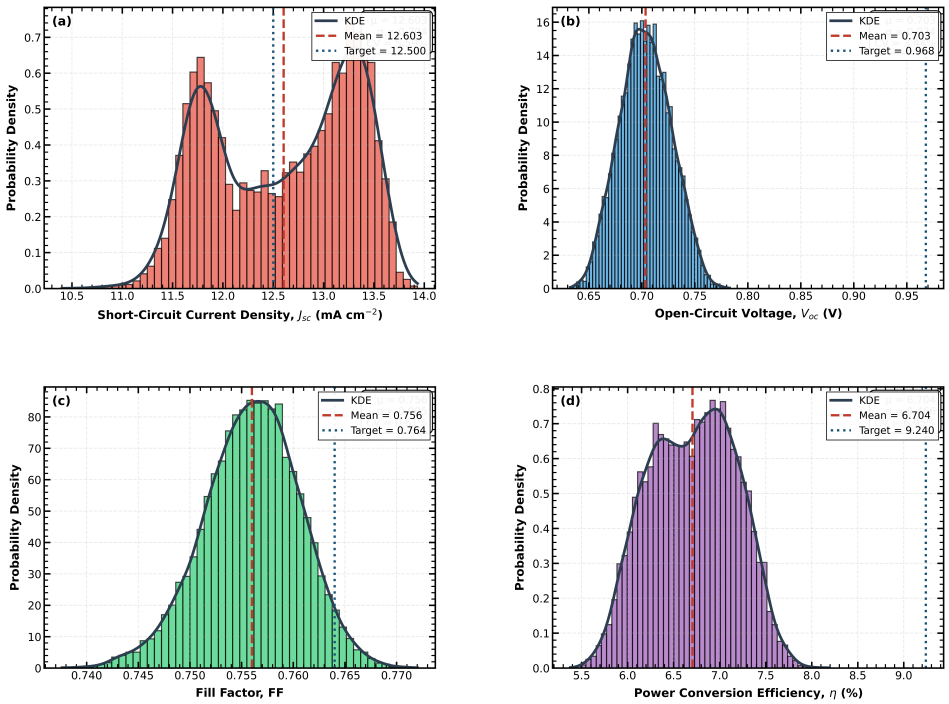

Figure 5: Statistical distributions from the Monte Carlo ensemble ($N = 5{,}000$), regenerated from an independent verification run of the Section 2.3 protocol using the single-diode model in Eq. 2. The input photocurrent distribution was $J_{sc,k} \sim \mathcal{N}(12.50, 0.59)$ mA cm^{-2}, with the electrical parameters fixed at their plasmonic values. (a) J_{sc}: $\mu = 12.50$ mA cm^{-2}. (b) V_{oc}: $\mu = 0.701$ V. (c) Fill factor: $\mu = 0.759$. (d) η: $\mu = 6.66\%$. Dashed lines indicate the ensemble means.

Table 3 summarizes the statistical metrics from the $N = 5{,}000$ Monte Carlo realizations with all electrical parameters held fixed at their optimized plasmonic values. Uncertainty in J_{sc} propagates to V_{oc} through $\delta V_{oc} =$

$(nk_BT/qJ_{sc})\,\delta J_{sc}$ and to η. Because R_s, R_{sh}, J_0, and n are fixed, the variability in FF is strongly suppressed by construction. The 95% intervals in Table 3 are prediction intervals for individual device realizations. This fixed-electrical-parameter analysis should therefore be interpreted as a best-case robustness bound; Section 3.5.1 relaxes the fixed-parameter assumption.

Table 3: Monte Carlo statistical summary ($N = 5{,}000$ realizations) for geometric variability only. Variability arises solely from the nanoparticle diameter and spacing distributions; all electrical parameters (J_0, n, R_s, and R_{sh}) are held fixed at their optimized plasmonic values. This is a best-case bound; see Section 3.5.1 for the extended analysis.

Parameter	**Mean**	**CV (%)**	**95% prediction interval**
J_{sc} (mA cm^{-2})	12.50	4.72	[11.34, 13.66]
V_{oc} (V)	0.7021	0.27	[0.6984, 0.7058]
FF	0.759	0.26	[0.755, 0.763]
η (%)	6.66	4.80	[6.05, 7.29]

$P(\eta > 6.0\%) = 84.3\%$; $P(\eta > 6.5\%) = 48.1\%$; $P(\eta > 7.0\%) = 8.0\%$; $P(\eta < \eta^{ref} = 4.30\%) < 0.01\%$.

Photocurrent variability.. Geometric fluctuations modulate the LSPR response. More than 99.9% of the realizations are reported to exceed the reference baseline ($J_{sc}^{ref} = 8.9$ mA cm^{-2}); this percentage should be verified against the raw Monte Carlo output rather than inferred solely from a fitted Gaussian approximation.

Fill-factor consistency.. The extremely low coefficient of variation in FF is a direct consequence of the Monte Carlo protocol: because all electrical parameters are held fixed, fill-factor variability is suppressed by construction. The

result demonstrates only that, within this fixed-electrical-parameter model, geometric variation does not substantially alter charge-extraction efficiency after the electrical parameters have been co-optimized.

Efficiency distribution.. The 95% prediction interval $\eta \in [6.05, 7.29]\%$ indicates that the modeled realizations remain above the reference efficiency under the stated assumptions. The strong J_{sc}–η correlation (Figure 6a, $r = 0.857$) identifies photocurrent as the primary modeled driver of efficiency. The moderate V_{oc}–η correlation ($r = 0.578$, Figure 6b) reflects the $V_{oc} \propto \ln(J_{sc})$ coupling inherent in the single-diode model. The moderate FF–η correlation ($r = 0.283$, Figure 6c) and the very weak linear association between J_{sc} and V_{oc} ($r = 0.085$, Figure 6d) further indicate that the optimized electrical design isolates the fill factor and voltage from optical-layer geometry in this conditional ensemble.

3.5.1. Extended Robustness Analysis Including Electrical-Parameter Variability

The analysis above isolates geometric variability by holding J_0, n, R_s, and R_{sh} fixed at their co-optimized plasmonic values, thereby providing a best-case robustness bound. To assess how additional sources of fabrication variability propagate to device performance, we repeat the Monte Carlo ensemble ($N = 5{,}000$) using the same single-diode formalism but sampling $J_0 \sim \text{LogNormal}(J_0^{plas}, \sigma \approx 28\%)$, $n \sim \mathcal{N}(1.55, 0.05)$, $R_s \sim \mathcal{N}(1.0, 0.15)$ Ω cm^2, and $R_{sh} \sim \text{LogNormal}(2500, \sigma \approx 22\%)$ Ω cm^2. These variables are sampled independently of the nanoparticle-geometry draw, and each realization's J–V curve is solved numerically using Brent's method for V_{oc} and the maximum-

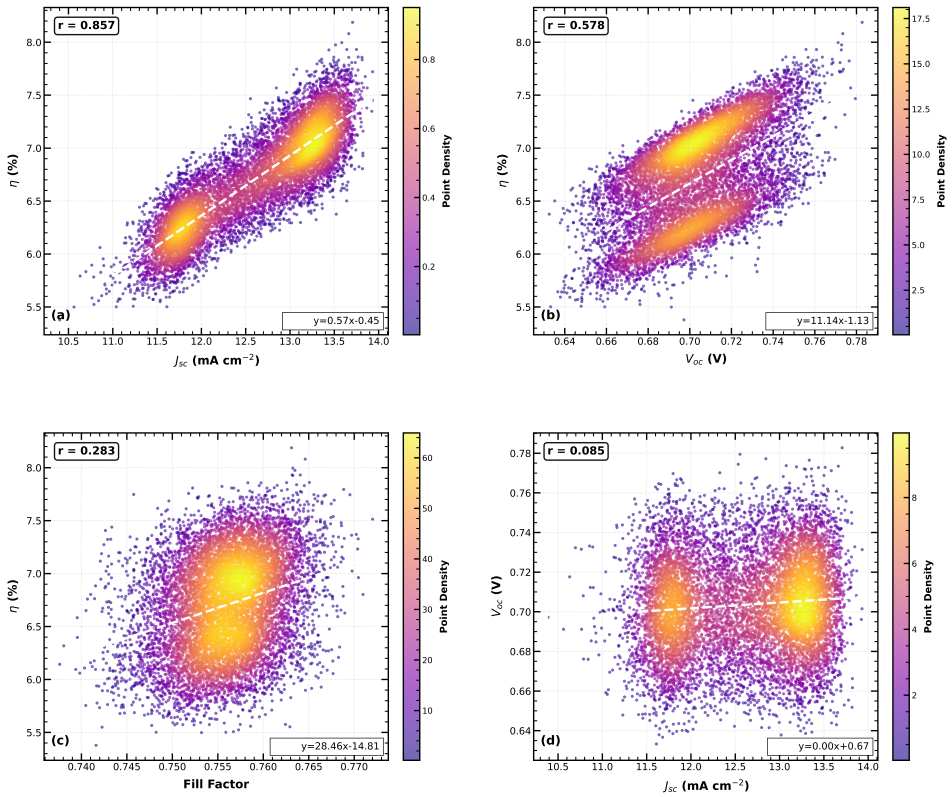

Figure 6: Parameter-correlation scatter plots from the Monte Carlo ensemble ($N = 5{,}000$ realizations). The color scale indicates the value of a third parameter. (a) J_{sc}–η correlation ($r = 0.857$, $R^2 = 0.734$), with points colored by fill factor; (b) V_{oc}–η correlation ($r = 0.578$), with points colored by J_{sc}; (c) FF–η correlation ($r = 0.283$), with points colored by V_{oc}; and (d) J_{sc}–V_{oc} association ($r = 0.085$), with points colored by η.

power point.

Table 4 summarizes the result. The efficiency coefficient of variation increases from approximately 5% with fixed electrical parameters to approximately 6.3% when the electrical parameters are variable. The fill-factor coefficient of variation rises from a few tenths of a percent to approximately 0.6%, and the 90% prediction interval widens to $\eta \in [5.97, 7.35]\%$. The modeled

devices remain above the reference baseline under the assumed distributions, but the 84.3% result at the 6.0% threshold in Table 3 is explicitly a best-case bound conditioned on ideal electrical co-optimization, not an unconditional manufacturing-yield forecast.

Table 4: Extended Monte Carlo robustness analysis ($N = 5{,}000$): geometric-only variability with fixed electrical parameters versus geometric plus electrical-parameter variability.

Metric	**Fixed electrical (best case)**	**Extended (electrical variable)**
V_{oc} CV (%)	0.27–0.28	3.6
FF CV (%)	0.05–0.26	0.62
η mean (%) / CV (%)	6.66 / 5.0	6.65 / 6.3
90% prediction interval for η (%)	–	[5.97, 7.35]
$P(\eta < \eta^{ref} = 4.30\%)$	$< 0.01\%$	$\approx 0\%$

A further simplification in both ensembles is the decoupling of optical and electrical variability. In practice, nanoparticle geometry and proximity to the ZnO/GaP and ITO/ZnO interfaces could plausibly modulate local trap density, interfacial strain, or contact quality, thereby coupling the geometric draw (d_k, s_k) directly to J_0, n, R_s, and R_{sh}. Capturing this coupling would require a combined FDTD–drift/diffusion framework rather than the surrogate-model plus single-diode approach used here. This is identified as a priority for future work.

4. Discussion

4.1. Context and Limits of Comparison

Quantitative comparison with published plasmonic photovoltaic studies requires matching the absorber bandgap, device architecture, illumination spectrum, active-area definition, electrical model, and whether the reported efficiencies are measured or simulated. The comparison table from the working draft is omitted because the cited examples do not provide a sufficiently verified, like-for-like basis for ranking the present model against those systems. A revised table should be added only after every row has been checked against the original paper and the metric definitions have been harmonized.

4.2. Subresonance Plasmonic Design Rationale

A notable feature of this design is that the LSPR resonance wavelength ($\lambda_{res} = 580$ nm) lies above the GaP absorption edge ($\lambda_{cut} = 549$ nm). This is an intentional consequence of the material system: 50-nm Au spheres in a ZnO/ZnS matrix with effective index $n_{eff} \approx 2.0$ exhibit a Mie dipolar resonance near 580 nm, consistent with the Fröhlich condition $\varepsilon_1(\lambda_{res}) = -2n_{eff}^2 = -8$ applied to Johnson–Christy Au optical constants [13]. Reducing the particle size to shift λ_{res} below 549 nm would require $d < 25$ nm, significantly reducing the extinction cross-section ($C_{ext} \propto d^6$ in the Rayleigh limit) and thus the near-field enhancement available to the absorber.

The chosen near-edge design is physically motivated by two properties of Au nanoparticle Mie extinction. First, the extinction spectrum has a broad spectral footprint: for 50-nm Au spheres, the FWHM of the extinction peak spans approximately 120 nm in ZnO [3]. Thus, at $\lambda = 500$ nm the near-

field enhancement may retain approximately 50% of its peak value, while at $\lambda = 420$ nm it may retain approximately 20–25%. When integrated over the absorption window and weighted by the AM1.5G photon flux [12], this behavior can yield a substantial photocurrent contribution. Second, indirect-gap compensation may be relevant because GaP's absorption coefficient, approximately $\alpha \approx 10^4$ cm^{-1} at 500 nm, decreases sharply near λ_{cut}. Positioning λ_{res} near the absorption edge may therefore concentrate near-field amplification in a spectral region where the intrinsic absorption is weakest.

Subresonance operation is a design hypothesis for the present GaP architecture. Its usefulness must be established from wavelength-resolved absorber absorption and the current integral, not inferred solely from the location or width of a metal-particle extinction peak.

4.3. Interpretation of Performance Correlations

In conventional plasmonic solar cells, negative correlations between J_{sc} and fill factor can arise because parameters that enhance light absorption, such as layer thickness or doping level, may simultaneously influence series resistance and recombination [22].

In this study, the Monte Carlo analysis in Section 3.5 deliberately varies only nanoparticle geometry while keeping all electrical parameters fixed. As a result, the dominant modeled association is between J_{sc} and efficiency ($r = 0.857$), indicating that photocurrent is the primary driver of efficiency in this ensemble. The moderate V_{oc}–η correlation ($r = 0.578$) arises naturally from the single-diode model: because $V_{oc} \propto \ln(J_{sc})$ for fixed J_0 and n, realizations with higher photocurrent also exhibit slightly higher open-circuit voltage. The moderate FF–η correlation ($r = 0.283$) reflects the weak dependence of

the fill factor on J_{sc} through the diode equation at fixed R_s and R_{sh}. The very weak J_{sc}–V_{oc} association ($r = 0.085$) should be interpreted only as a statistical property of the reported ensemble and not as evidence that the physical voltage is independent of photocurrent.

Taken together, this analysis indicates that, with the assumed optimized electrical design ($R_s = 1.0\ \Omega\ \mathrm{cm}^2$, $R_{sh} = 2500\ \Omega\ \mathrm{cm}^2$), fabrication-induced variations in the plasmonic layer primarily affect J_{sc}, whereas FF and V_{oc} remain nearly constant under the fixed-electrical-parameter assumption. This is a practically relevant but conditional indicator of robustness; the extended analysis in Section 3.5.1 shows that electrical variability broadens the efficiency distribution.

4.4. Limitations and Scope

Several limitations should be noted. First, all results are theoretical and have not been validated experimentally. Fabricated devices may exhibit higher interface-defect densities, nanoparticle aggregation, or parasitic absorption effects that are not captured in the simulations. Second, the surrogate model assumes ideal spherical nanoparticles with a uniform random spatial distribution characterized only by its mean interparticle spacing. Near-field coupling at very small interparticle spacings is therefore not fully represented. In a real random spatial distribution, the tail of the pair-distance distribution can place a non-negligible fraction of particles in locally clustered configurations with gaps well below the 59-nm mean surface-to-surface spacing, even when the ensemble-average volume fraction is consistent with $f_v = 5\%$. Such clustering could increase local near-field enhancement at clustered sites through gap-mode plasmons, but this benefit could be offset

by increased parasitic absorption in the metal and reduced effective coverage elsewhere. Quantifying this trade-off requires FDTD simulations resolved over an explicit pair-correlation function.

Third, the Monte Carlo protocol decouples optical and electrical variability. In practice, nanoparticle geometry and proximity to the ZnO/GaP and ITO/ZnO interfaces could plausibly modulate local trap density, interfacial strain, or contact quality and thereby couple the geometric draw (d_k, s_k) to J_0, n, R_s, and R_{sh}. Capturing this effect would require a coupled FDTD–drift/diffusion framework. Fourth, the relatively low V_{oc} of approximately 0.70 V indicates substantial voltage losses; however, the present model does not establish that interfacial recombination is the unique dominant mechanism. Higher voltages would require improved passivation, reduced defect density, or alternative heterojunction designs beyond the scope of this work.

5. Conclusion

This work presents a model-based framework for assessing plasmonic enhancement in wide-bandgap III–V photovoltaic devices while explicitly distinguishing photocurrent benchmarking from overall efficiency benchmarking. Three main conclusions follow.

First, the nominal model outputs increase J_{sc} from 8.9 to 12.5 mA cm^{-2}, corresponding to 92.6% of the adopted Shockley–Queisser photocurrent benchmark for GaP. This result does not imply comparable proximity to the overall Shockley–Queisser efficiency limit. As quantified in Section 3.1.1, the modeled plasmonic efficiency is approximately 31% of the cited radiative-limit efficiency, and the remaining gap is dominated by the low modeled open-

circuit voltage. The electrical parameters are calibration assumptions rather than outputs of the optical simulation, and J_0 has been calculated using the complete open-circuit condition, including finite shunt leakage. The reported voltage should nevertheless be reproduced from the unrounded parameter set used in the numerical implementation.

Second, the modeled open-circuit voltage of approximately 0.70 V remains far below the cited radiative-limit voltage. This result is consistent with substantial voltage losses, potentially including nonradiative recombination, although the present optical calculation and single-diode fit do not identify the microscopic loss mechanism. The assumed co-optimized electrical parameter sets use $J_0 = 1.51 \times 10^{-9}$ and 3.02×10^{-10} A cm^{-2} and ideality factors of 1.75 and 1.55, respectively. These values are model inputs rather than direct outputs of the optical simulation. A microscopic attribution of the improvement to ZnS passivation therefore requires device-level evidence.

Third, the Monte Carlo analysis with $N = 5{,}000$ realizations indicates that, when the optimized electrical parameters are held fixed, nanoparticle-geometry variations primarily affect J_{sc}, which has a coefficient of variation of 4.72%, whereas the fill factor remains nearly constant, with a coefficient of variation of 0.26%. Under these conditional assumptions, 84.3% of realizations exceed 6.0% efficiency. When electrical-parameter variability is included, the efficiency distribution broadens and its coefficient of variation increases to approximately 6.3%. Accordingly, the 84.3% figure should be interpreted as a best-case conditional probability rather than as an unconditional estimate of experimental manufacturing yield.

5.1. Experimental Roadmap

The immediate objective should be controlled validation rather than direct transfer of the present point estimates to a fabrication target. First, the optical model should be reproduced using documented solver settings, optical constants, mesh-convergence criteria, source conditions, and absorber-specific absorption spectra. Second, a device-level electrical model should establish the reference and optimized values of n, J_0, R_s, and R_{sh} on the basis of a clearly stated physical or experimental rationale. Third, the optical and electrical counterfactual cases should be evaluated using identical numerical procedures. Only after these steps should the proposed architecture be fabricated and measured under calibrated AM1.5G illumination. Until then, the reported values should be interpreted as model-dependent estimates rather than guaranteed experimental targets.

5.2. Future Directions

The framework developed in this work suggests several directions for further research: (i) exploring alternative nanoparticle geometries, such as nanorods or nanostars, to achieve broader spectral enhancement; (ii) integrating GaP top cells in tandem with Si or perovskite bottom cells for improved overall efficiency; (iii) implementing hot-carrier extraction schemes to utilize plasmonically generated carriers before thermalization; (iv) experimentally validating the predicted robustness through statistically guided fabrication campaigns; and (v) expanding the surrogate-model training set to a 7×7 or 9×9 FDTD grid with an explicit convergence study. Future work should also resolve the Monte Carlo geometric ensemble using an explicit pair-correlation function, replace asymptotic arguments with directly

measured convergence and clustering-sensitivity curves, and couple geometric and electrical Monte Carlo draws through a joint FDTD–drift/diffusion framework.

Funding Statement

This research did not receive any specific grant from funding agencies in the public, commercial, or not-for-profit sectors.

References

[1] H. A. Atwater, A. Polman, Plasmonics for improved photovoltaic devices, Nature Materials 9(3) (2010) 205–213.

[2] K. Catchpole, A. Polman, Plasmonic solar cells, Optics Express 16(26) (2008) 21793–21800.

[3] J. A. Schuller, E. S. Barnard, W. Cai, Y. C. Jun, J. S. White, M. L. Brongersma, Plasmonics for extreme light concentration and manipulation, Nature Materials 9(3) (2010) 193–204.

[4] A. Ali, F. El-Mellouhi, A. Mitra, B. Aïssa, Research progress of plasmonic nanostructure-enhanced photovoltaic solar cells, Nanomaterials 12 (2022) 788.

[5] S. Jiang, W. Yang, A. Zhu, Structure–function tailoring of plasmonic nanomaterials for thin-film photovoltaics, Carbon Energy 8 (2026) e70239. https://doi.org/10.1002/cey2.70239.

[6] A. G. Waketola, C. Pfukwa, P. Neethling, G. Bosman, Z. Genene, E. Wang, W. Mammo, F. G. Hone, N. A. Tegegne, Embedding plasmonic gold nanoparticles in a ZnO layer enhanced the performance of inverted organic solar cells, RSC Advances 13(24) (2023) 16175–16184.

[7] S. Rühle, Tabulated values of the Shockley–Queisser limit for single-junction solar cells, Solar Energy 130 (2016) 139–147.

[8] W. Shockley, H. J. Queisser, Detailed balance limit of efficiency of p–n junction solar cells, Journal of Applied Physics 32(3) (1961) 510–519. https://doi.org/10.1063/1.1736034.

[9] S. K. Mishra, et al., Plasmonic solar energy harvesting by ZnO nanostructures and their composite interfaces: a review, Energy Technology 11 (2023) 2201393.

[10] D. Zagorac, J. Zagorac, M. Pejić, B. Matović, J. C. Schön, Band gap engineering of newly discovered ZnO/ZnS polytypic nanomaterials, Nanomaterials 12(9) (2022) 1595.

[11] A. Agarwal, G. Misra, K. Agarwal, Semiconductor III–V nanowires: synthesis, fabrication and characterization of nanodevices, Journal of The Institution of Engineers (India): Series B 103(2) (2022) 699–709.

[12] C. A. Gueymard, D. Myers, K. Emery, Proposed reference irradiance spectra for solar energy systems testing, Solar Energy 73(6) (2002) 443–467. https://doi.org/10.1016/S0038-092X(03)00005-7.

[13] P. B. Johnson, R.-W. Christy, Optical constants of the noble metals, Physical Review B 6(12) (1972) 4370.

[14] J. Nelson, The Physics of Solar Cells, Imperial College Press, London, 2003.

[15] L. M. P. Deotti, I. C. da Silva Junior, A survey on the parameter extraction problem of the photovoltaic single-diode model from a current–voltage curve, Solar Energy 263 (2023) 111930. https://doi.org/10.1016/j.solener.2023.111930.

[16] H. Li, S. Yang, J. Hu, Z. Zhang, P. Tang, Y. Jiang, L. Tang, B. Zou, Which method is more efficient on enhancing light absorption for silicon nanowire array-based solar cells: plasmonic metal nanoparticles or narrow-bandgap semiconductor quantum dots?, Materials Science in Semiconductor Processing 146 (2022) 106661.

[17] I. Zamkoye, B. Lucas, S. Vedraine, Synergistic effects of localized surface plasmon resonance, surface plasmon polariton, and waveguide plasmonic resonance on the same material, Nanomaterials 13 (2023) 2209.

[18] A. Amirjani, S. K. Sadrnezhaad, Computational electromagnetics in plasmonic nanostructures, Journal of Materials Chemistry C 9 (2021) 9791–9819. https://doi.org/10.1039/D1TC01742J.

[19] M. A. Green, Solar cell fill factors: general graph and empirical expressions, Solid-State Electronics 24(8) (1981) 788–789.

[20] O. D. Miller, A. G. Polimeridis, M. T. Homer Reid, C. W. Hsu, B. G. DeLacy, J. D. Joannopoulos, M. Soljačić, S. G. Johnson, Fundamental limits to optical response in absorptive systems, Optics Express 24(4) (2016) 3329–3364. https://doi.org/10.1364/OE.24.003329.

[21] M. Panish, H. Casey Jr, Temperature dependence of the energy gap in GaAs and GaP, Journal of Applied Physics 40(1) (1969) 163–167.

[22] A. Polman, H. A. Atwater, Photonic design principles for ultrahigh-efficiency photovoltaics, Nature Materials 11(3) (2012) 174–177.